

Compact pulse position control-based inverter for high efficiency inductive power transfer to electric vehicle

ISSN 1755-4535

Received on 17th June 2019

Revised 10th September 2019

Accepted on 2nd October 2019

E-First on 27th November 2019

doi: 10.1049/iet-pe.2019.0720

www.ietdl.org

Sooraj Varikkottil¹, Febin Daya J.L.¹ ✉¹School of Electrical Engineering, Vellore Institute of Technology, Chennai, India

✉ E-mail: febinresearch@gmail.com

Abstract: A compact high efficient inductive power transfer (IPT) topology based on pulse position control is proposed for wireless charging of electric vehicle. Near-field wireless charging is efficiently achieved by the resonance-enhanced IPT technique. The system sustains high power transfer efficiency under contingency in misalignment of pickup coil and load variations. The performance evaluation of the proposed system under the occurrence of anticipated perturbation in load and mutual inductance is studied numerically. Experimental results from the developed prototype corroborate the theoretical and simulated results discussed in the proposed study.

1 Introduction

Inductive power transfer (IPT) is one of the efficient and effective techniques used in wireless power transfer (WPT) system [1–5]. This innovation got a wide assortment of utilisation like wireless charging of mobile phone, laptops, electric vehicle etc. [4–7]. Static and dynamic wireless charging methods provide a permanent solution to the range of travel and charging time of the electric vehicle [8, 9]. This new method of transportation is clean and safe mode of transport in which, automatic charging facilities and opportunity charging has an attracting feature.

Power electronic converter topologies play a significant role in efficient power transfer in the system. Semiconductor switches are deployed in different fashion along with the energy storage elements in order to get the desired output response. The arrangement of energy storage elements along with the semiconductor switches brings new possibility in the higher order resonance, thereby increases the power transfer capability of the system. Moreover, the existing predominant topologies are sizable due to the presence of separate inverter and converter stages [1, 2]. This also increases the cost of the system. In case, the inverter is inherent with the energy storage element and the combination is enough to make the resonance then the system will outperform better than the conventional one.

The performance of the system gets affected by changes in load, frequency and the contingency in misalignment of the pickup coil [10]. The distance of power transfer is limited by the size and shape of the coil [11–13]. Generally, the circular copper coil is mounted on the ferrite spokes in order to enhance maximum flux linkage [14–16]. This higher order decoupled circuit creates resonance to transfer power from one circuit to the other with a larger air gap [15]. Primary inductive coil with low internal resistance should take more current to develop the induced voltage on the other coil. Recent research progress on LCL-based topologies along with H-bridge inverters got wide acceptance in the current scenario [17–20]. The existing conventional circuit topologies are predominant and widely accepted. The possibility of combination in resonance is still open in these circuit topologies. However, the power transfer efficiency will be high only when the losses are minimum.

Retraction of semiconductor switches from the existing topologies will improve the efficiency, but it will affect the mode of operation. Class E-based resonance topologies use single semiconductor switches for the inverting purpose, which reduces the conduction and switching losses in the network [20, 21]. Since the operating frequency of the system is very high, class E-based

converters are not possible to use for electric vehicle charging as per SAE J2954 standards. In other words, the secondary quality factor needs to be more than seven to achieve good power transfer efficiency in case of class E-based converter [21, 22]. Misalignment of the coil and the loading will affect the power transfer rate and efficiency in class E WPT system [23–26]. Higher the switching frequency, higher the losses and the total harmonic distortion (THD) of input current is very high, which is burden to the supply.

In this paper, a new converter topology is proposed for wireless charging of electric vehicle based on the resonance-enhanced IPT technique with reduced number of semiconductor switches. The proposed system is very compact, efficient and shows stable performances under mutual inductance and load variations. The conventional inverters operate based on the width of the pulses or in other ways it depends on the duty ratio. However, the proposed inverter operates based on the position of pulses. The voltage and current are regulated based on the phase-shift time delay (t_d) between the semiconductor switches S_1 and S_2 . The system gives high power transfer efficiency with minimum coupling at 85 kHz operating frequency. The changes in efficiency are minimum for the large range of coupling coefficient, thereby preferable for dynamic perturbations. Hence, it is suitable for dynamic IPT system.

2 Proposed IPT architecture

The proposed new IPT topology with reduced semiconductor switches are shown in Fig. 1. These switches operate at 85 kHz switching frequency along with the hybrid resonance topology. A secondary resonance circuit along with an uncontrolled rectifier is connected to the load through the low pass filter. The steady-state equivalent resistance of the battery bank is considered as the load in this system. Charging current of the inductor L_c with the pulse position is shown in Fig. 2a. As shown in Fig. 2a, the current is initiated by the rising edge of pulse G_1 and the current decayed from the rising edge of the pulse G_2 . The proposed IPT system is further simplified into Fig. 2b by referring the reflective capacitor ($C_r(M, R_{eq})$) and the resistor ($R_r(M, R_{eq})$) to the primary side. Similarly, a decoupled secondary circuit is also made to simplify the analysis on the secondary side of the circuit, where the open-circuit voltage (V_{oc}) depends on the primary current flowing through the inductive coil (I_p). The different mode of operation of the proposed system is shown in Fig. 3.

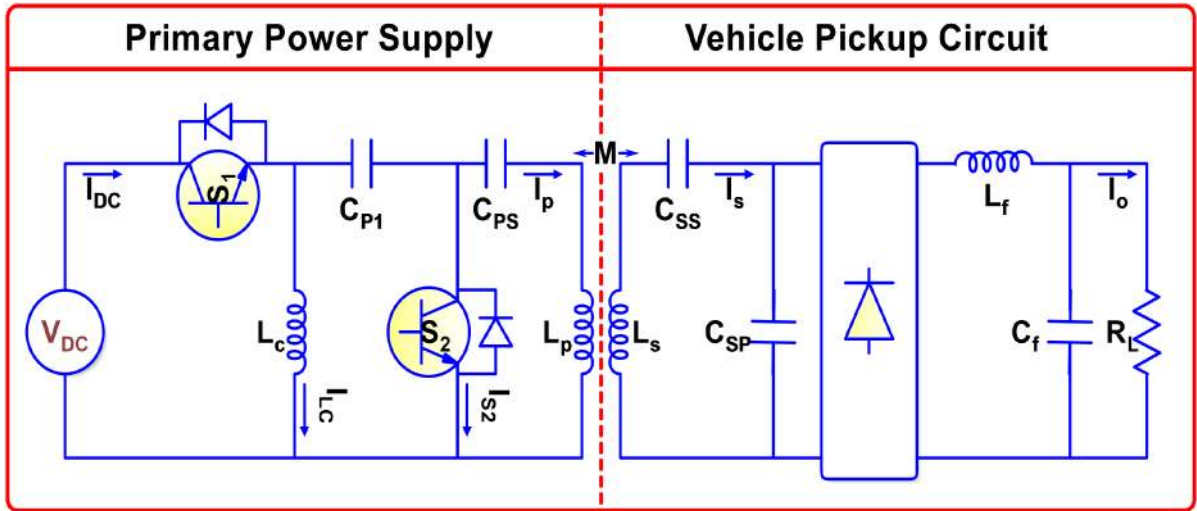


Fig. 1 Proposed IPT system

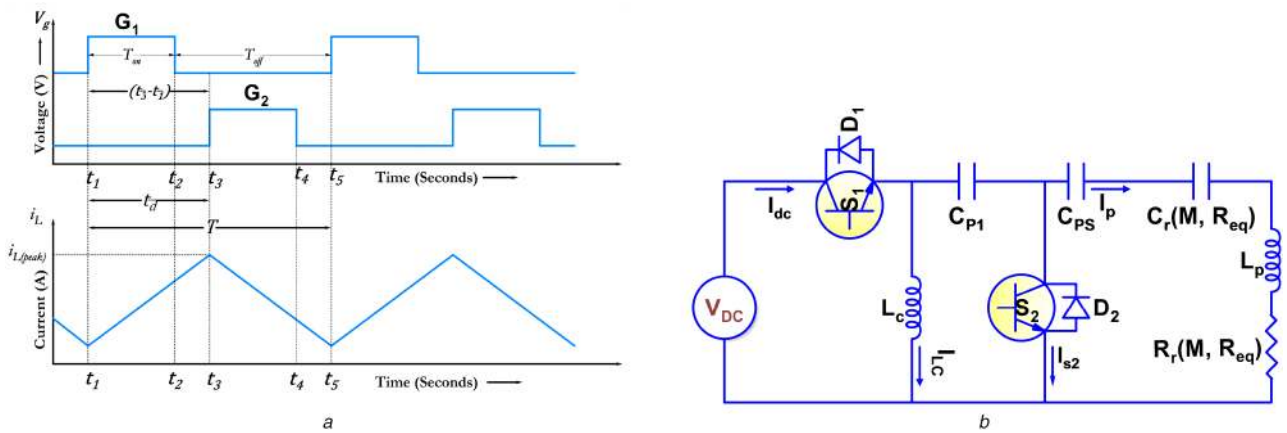


Fig. 2 Pulse position and simplified equivalent circuit
 (a) Pulse position and charging current through the inductor L_c , (b) Simplified equivalent circuit

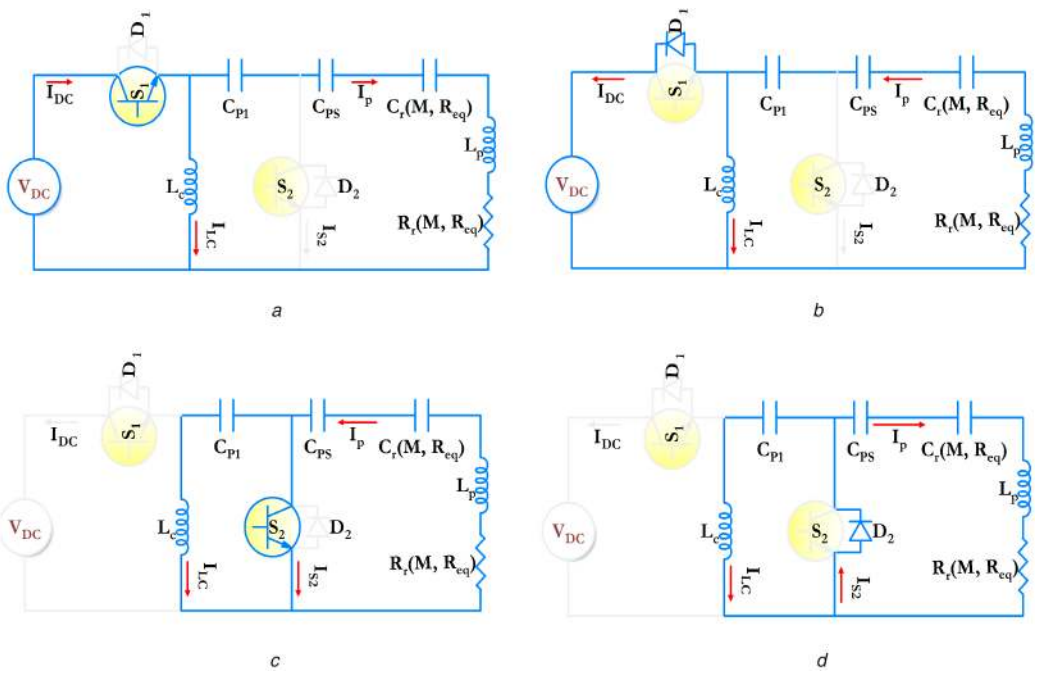


Fig. 3 Mode of operation with a simplified equivalent circuit
 (a) Mode 1, (b) Mode 2, (c) Mode 3, (d) Mode 4

2.1 Simplified equivalent circuit

The entire IPT system is simplified and shown in Fig. 2b. The reflected capacitor ($C_r(M, R_{eq})$) in terms of secondary circuit elements are written as

$$C_r(M, R_{eq}) = \frac{R_{eq}^2(w^2 C_{sp} L_{seq} - 1)^2 + (w L_{seq})^2}{(w^4 M^2)[C_{sp} R_{eq}^2 (w^2 C_{sp} L_{seq} - 1) + L_{seq}]} \quad (1)$$

The reflected resistance ($R_r(M, R_{eq})$) in terms of secondary linear circuit elements are written as

$$R_r(M, R_{eq}) = \frac{R_{eq}(wM)^2[w^2 C_{sp} L_{seq} - (w^2 C_{sp} L_{seq} - 1)]}{R_{eq}^2(w^2 C_{sp} L_{seq} - 1)^2 + (w L_{seq})^2} \quad (2)$$

where M is the mutual inductance between the primary and secondary coil and the secondary equivalent inductance L_{seq} is written as

$$L_{seq} = L_s - \frac{1}{w^2 C_{ss}} \quad (3)$$

The resonance frequency w is written in terms of secondary circuit element as

$$w = \frac{1}{\sqrt{L_{seq} C_{sp}}} \quad (4)$$

Similarly, the primary equivalent inductance is written as

$$L_{peq} = L_p - \frac{1}{w^2 C_{ps}} - \frac{1}{w^2 C_r} \quad (5)$$

Primary equivalent inductance is represented in terms of capacitors C_{ps} and C_r .

2.2 Mode of operation and steady-state analysis

Mode of operation of the converter is explained in the simplified equivalent circuit.

2.2.1 Mode 1: The switch S_1 is turned on and inductor L_c is charging. Meanwhile, the remaining current is drawn by the branch containing primary inductance. Mode 1 is shown in Fig. 3a.

2.2.2 Mode 2: The switch S_1 is turned off and diode D_1 is forward biased. Inductor L_c continues to be in charge and the current I_p reverse its direction with respect to the previous modes. Mode 2 is shown in Fig. 3b.

2.2.3 Mode 3: During this mode, the switch S_2 is turned on and the D_1 is reverse biased. Current I_p maintain its direction with respect to the previous modes. Inductor L_c discharges its current through the primary track. Mode 3 is shown in Fig. 3c.

2.2.4 Mode 4: In this mode, the switch S_2 is turned off and the diode D_2 is forward biased. Inductor L_c continues to discharge through the diode. Current I_p reverse its direction with respect to the previous modes. Mode 4 is shown in Fig. 3d.

When switch S_1 is turned on

$$V_{dc} = L_c \frac{di_L}{dt} \quad (6)$$

The current through inductor flow through switch S_1 till t_2 . Further, the diode D_1 is forward biased till t_3 . Assuming the drop across the switch and diode are zero during the turn on time of the respective devices. The current ripple during the period t_1 - t_3 is written as

$$\Delta i_L = \left(\frac{V_{dc}}{L_c}\right)(t_3 - t_1) \quad (7)$$

Similarly, during the period t_3 - t_5 , the current ripple is written as

$$\Delta i_L = -\left(\frac{V_{C_{p1}}}{L_c}\right)(t_5 - t_3) \quad (8)$$

Current through the inductor will not change suddenly $i_L(0^-) = i_L(0) = i_L(0^+)$. Similarly, the voltage across the capacitor will not change suddenly $v_C(0^-) = v_C(0) = v_C(0^+)$. The voltage across capacitor C_{p1} is written as

$$V_{C_{p1}} = -V_{dc} \left(\frac{t_3 - t_1}{t_5 - t_3}\right) \quad (9)$$

The voltage across the capacitor is dependent upon the pulse position t_d of the pulse. However, pulse width should be maintained until the conduction is achieved.

The voltage across the capacitor in terms of phase delay (t_d) is written as

$$V_{C_{p1}} = -V_{dc} \frac{t_d}{T - t_d} \quad (10)$$

For $t_d = T/2$ the voltage across $V_{C_{p1}}$ will be

$$V_{C_{p1}} = -V_{dc} \quad (11)$$

This is the preferred operating condition irrespective of the duty ratio. This is one of the key benefits of the proposed system. Now, from the above expression it is inferred that the voltage across the inductor L_c is written as

$$v_L(t) = \begin{cases} V_{dc}; & t_1 < t < t_3 \\ -V_{dc} \left(\frac{t_d}{T - t_d}\right); & t_3 < t < t_5 \end{cases} \quad (12)$$

The current through the inductor L_c is written as

$$i_L(t) = \begin{cases} \left(\frac{V_{dc}}{L_c}\right)t; & t_1 < t < t_3 \\ \left(\frac{V_{C_{p1}}}{L_c}\right)t; & t_3 < t < t_5 \end{cases} \quad (13)$$

Then the root mean square (RMS) voltage across the inductor L_c is

$$V_{L_{rms}} = \sqrt{\frac{1}{T} \left[\int_{t_1}^{t_3} (V_{dc})^2 + \int_{t_3}^{t_5} \left(-V_{dc} \left(\frac{t_d}{T - t_d}\right)\right)^2 dt \right]} \quad (14)$$

When $t_d = T/2$, irrespective of the duty ratio, the RMS voltage across the inductor will be the V_{dc} only. Hence, when S_2 and D_2 are in off state (mode 1 and mode 2), the KVL of the simplified equivalent circuit will be

$$V_{dc} = V_{C_{p1}} + V_{C_{ps}} + V_{C_r} + V_{L_p} + V_{R_r} \quad (15)$$

The capacitor C_{ps} is designed to be in resonance with L_c and the switch S_2 is operated in such a way that $-V_{dc}$ appears across the capacitor C_{p1} during the negative slope of the current passing through the charging inductor. Hence, approximately, RMS voltage across the inductor (L_c) is the same as the supplied DC voltage (V_{dc}).

An equivalent capacitance can be made out of the three series capacitance from the equivalent circuit. Hence, C_{eq} is the equivalent series capacitance of C_{p1} , C_{ps} and C_r . If V_s is the

approximate RMS value corresponding to the V_{dc} , then the current I_p flowing through the primary track will be

$$I_p = \frac{V_{dc} \omega C_{p1}}{R_r \omega C_{p1} - j(1 - \omega^2 C_{p1} L_{peq})} \quad (16)$$

If C_{p1} and primary equivalent inductance (L_{peq}) is at resonance, the term $1 - \omega^2 C_{p1} L_{peq}$ approaches to zero and the second term in denominator vanishes. Hence, maximum current will flow through the circuit, which will develop a maximum voltage across the inductor.

2.3 Secondary decoupled circuit

The secondary decoupled circuit shown in Fig. 4 separates the secondary circuit topology along with a secondary induced voltage from the primary circuit.

The open-circuit voltage V_{oc} is written as

$$V_{oc} = j\omega M I_p \quad (17)$$

Equivalent resistance is formed instead of the non-linear semiconductor switches under steady-state operating condition of the device in terms of load resistance.

$$R_{eq} = \frac{\pi^2 R_L}{8} \quad (18)$$

The current follows through the secondary circuit will be

$$I_s = \frac{R_{eq} M I_p}{j\omega L_{seq} + R_{eq}(1 - \omega^2 L_{seq} C_{sp}) L_{seq}} \quad (19)$$

The voltage across the secondary parallel capacitor C_{sp}

$$V_{C_{sp}} = \frac{\omega R_{eq} L_{seq} M I_p}{j\omega L_{seq} + R_{eq}(1 - \omega^2 L_{seq} C_{sp}) L_{seq}} \quad (20)$$

I_p is represented in terms of V_{dc} in which implies that the voltage across the secondary capacitor $V_{C_{sp}}$ and R_{eq} is a function of V_{dc} .

2.4 Analysis of waveform

The instantaneous current and voltage waveform of the circuit elements are derived in order to validate the magnitude and phase of the different waveform. The current through the primary inductor (L_p) is taken as reference in this case

$$i_p(t) = I_{pm} \sin \omega t \quad (21)$$

The primary current lag the voltage by 90° . Since the current is taken as reference, the voltage across the primary inductor (L_p) is written as

$$v_{L_p}(t) = \omega L_p I_{pm} \sin\left(\omega t + \frac{\pi}{2}\right) \quad (22)$$

Current through the secondary inductor with respect to the primary current is written as

$$i_s(t) = I_{sm} \sin(\omega_0 t - \phi) \quad (23)$$

The secondary current $i_s(t)$ is shifted by the angle ϕ with respect to the primary current.

Where ϕ is written as

$$\phi = -\tan^{-1} \left\{ \frac{\omega L_{seq}}{R_{eq}(1 - \omega^2 L_{seq} C_{sp})} \right\} \quad (24)$$

Similarly, the voltage across the secondary pickup coil is written as

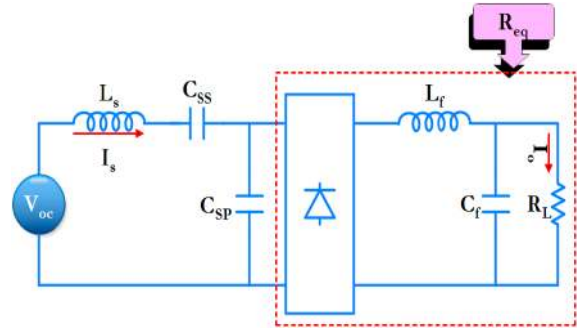


Fig. 4 Secondary decoupled circuit

$$v_{L_s}(t) = \omega L_p I_{pm} \sin\left(\omega t + \frac{\pi}{2} - \phi\right) \quad (25)$$

The angle ϕ is negative according to (24). This indicates that the voltage across the secondary inductor shifts $>90^\circ$ and $\leq 180^\circ$ with respect to the V_{L_p} . The current through the different switches are the portion of sinusoidal waveform due to the different energy storage elements. Similarly, the current through switch S_1 is written as

$$i_{dc}(t) = I_{pm} \sin \omega t + i_{lc}(t) \quad (26)$$

for the period, t_1-t_3 . Similarly, the instantaneous current through the switch S_2 is written as

$$i_{s2}(t) = I_{pm} \sin \omega t - i_{lc}(t) \quad (27)$$

Further, simulation studies have been carried out to substantiate the theoretical findings.

3 Simulation studies

The developed equivalent circuit of the proposed system is simulated and performances are studied under variations in load and mutual inductance. The notion in the theoretical aspects is endorsed along with the simulation results. Fig. 5 shows the current waveform through different energy storage elements at minimum coupling coefficient. The injection of current into the primary inductive track is controlled by two semiconductor switches which are operated alternatively to meet the purpose. The current through the inductor is continuous in nature and works in continuous conduction mode. The voltage waveform of different energy storage elements in the system is shown in Fig. 6. It is observed that the voltage across inductor L_c is, approximately, square-shaped and the amplitude is same as supply voltage. Hence, the RMS value of the voltage waveform will be maximum value of the square waveform. Voltage and current waveform at output and input are shown in Fig. 7. The system is designed for delivering 1 kW to the load at minimum coupling of 0.1245. The power transfer efficiency increases with increase in coupling coefficient. The current and the voltage waveforms of different energy storage elements are observed under contingency in misalignment and load variations. The load resistance is varied from 10–20 Ω . Variation in misalignment is considered in the range of 0.1–0.3, which comes under loosely coupled IPT system. The internal resistance of inductors is taken into account for simulation studies. The equivalent series resistor of the capacitors is neglected since it is very less compared to the internal resistance of the inductor.

The inverter is operated with 85 kHz operating frequency. A 220 V input DC voltage is used to deliver 1 kW output power to the load at the minimum coupling coefficient of 0.1245. This loosely coupled IPT system gives high efficiency due to the reduced number of semiconductor switches even under lower switching frequency compared to the other topologies [1, 2].

It is observed that the operating region is best suited in the near resonance region. The proposed topology exhibits high-power transfer efficiency throughout the variation in coupling factor compared to the conventional LCL architecture [1]. This has been

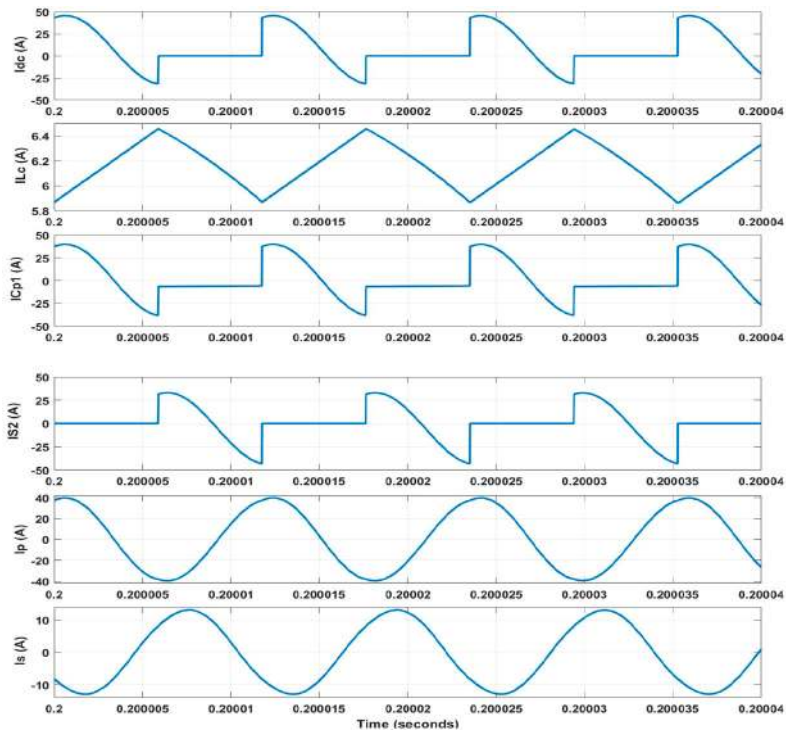


Fig. 5 Simulated current waveform through various circuit elements

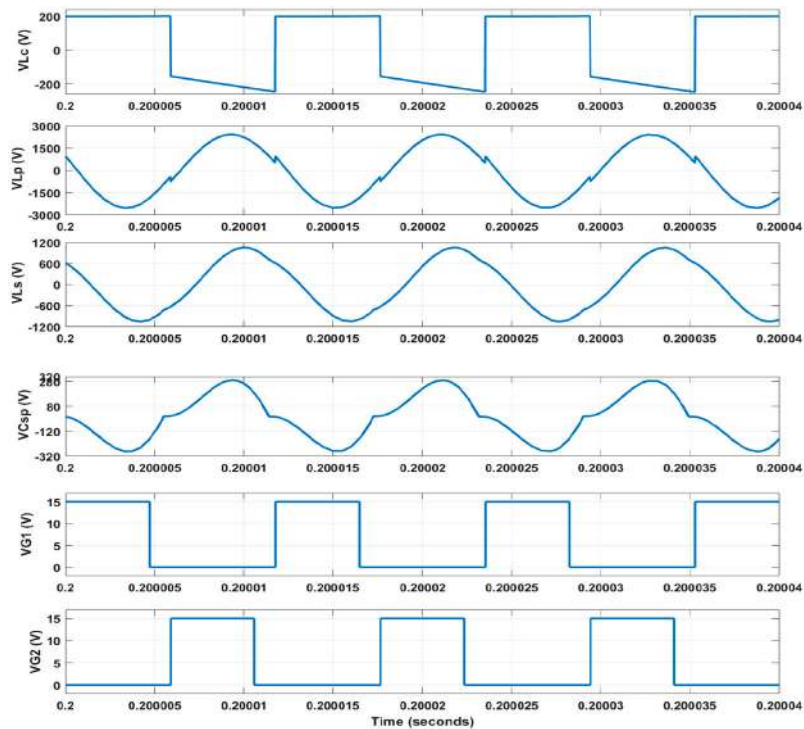


Fig. 6 Simulated voltage waveform across various circuit elements

validated for different values of mutual inductance. This makes the system more reliable under practical working conditions and also will be a suitable converter for the dynamic IPT systems. The system is operated over a range of frequency from 81.5 to 90 kHz as per SAEJ2954 standards and it is observed that efficiency was almost constant compared to the conventional LCL topology.

The performance of the system is observed in various case studies. Based on the simulated data, few relevant graphs are plotted in order to infer the reliability aspect of the system. Table 1 shows the values of circuit parameters considered for simulation and experimental studies. The simulation studies are carried out with the most realistic data, such that the exact behaviour of the system is obtained.

3.1 Case studies

The performance evaluation of the proposed topology is evaluated on comparing with the existing conventional LCL architecture. Both the circuits have been designed for 1 kW and simulated in MATLAB platform. The internal resistance of inductors and semiconductor switches are considered for evaluation. It has been observed that the variation in load and mutual inductance are the contingent course of action, where the probability of perturbation in the values of mutual inductance and load resistance are unpredictable. Hence, case studies are carried out with a variation in load and mutual inductance. Figs. 8a and b represents the variation in voltage and efficiency gains to the coupling coefficient

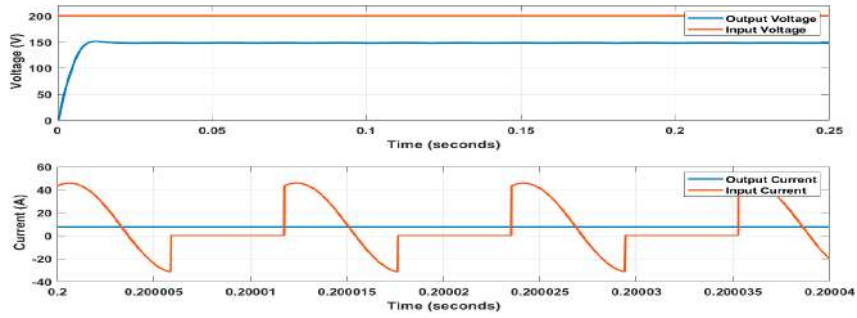


Fig. 7 Output and input voltage, current waveform

Table 1 Values of the circuit element

Parameter	Value
power	1 kW
frequency (w)	85 kHz
L_c	2000 μ H
C_{p1}	200 nF
C_{ps}	75 nF
L_p	110 μ H
L_s	110 μ H
C_{ss}	85 μ F
C_{sp}	50 μ F
L_f	135 μ H
C_f	2500 μ F
k_{min}	0.1245
controller	Texas Instrument C2000 Delfino TMS320F28377S Controller
MOSFET	SPW47N60C3
$R_{ds_{on}}$	0.07 Ω
rL_b	0.3 Ω
diode	MUR1560G (high speed switching diode)
battery	lithium ion
RF module	433 MHz, STX882
gate driver	IR2110

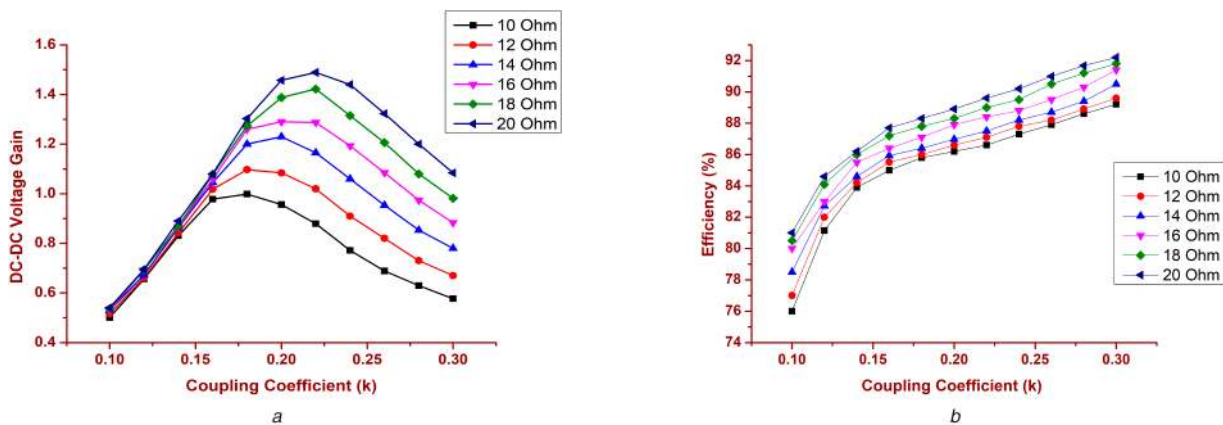


Fig. 8 Voltage gain and efficiency of the proposed system under various coupling coefficients
 (a) Voltage gain against coupling coefficient, (b) Efficiency against coupling coefficient

and load changes. The obtained results are further looked in detail to analyse the performance of the converter.

3.1.1 Under variation of load: The load for the proposed IPT system is the battery. The steady-state equivalent resistance of the battery is considered as a load for the system. Connected number of batteries and charging current vary depending upon the type and the manufacturer of the vehicle. Hence, variation in connected load from the converter end is expected. Conventional LCL topology, as well as proposed topology, are subjected to load variation from 10 to 20 Ω . This range is selected because of the ratio of average

terminal voltage to the charging current of the available batteries used in the electric vehicle. The obtained results are plotted as a graph as shown in Fig. 8. The load current fluctuates as per the load, relatively the input current drawn from the supply also changes. The efficiency of the proposed converter varied from 76 to 92.1%. However, the conventional LCL efficiency varied from 75.62 to 87.94%. Additionally, for the proposed topology, voltage gain shifts from 0.45 to 1.53 amid the time of load variation. Similarly, the conventional LCL voltage gain shifts from 0.38 to 0.533 amid a similar period. When all is said in done, the voltage gain and efficiency increases while there is an increase in load

resistance. In another way, the proposed topology gives better efficiency for the lighter load applications. The power delivered to the load increases while there is an increase in load resistance.

3.1.2 Under misalignment of pickup coil: The contingency in misalignment is another unpredictable event for the system. Depending upon the clearance and the position of the pickup coil from the primary coil, the misalignment occurs. The proposed system is simulated with different mutual inductances along with the conventional LCL architecture and judged at the execution. The values of reflected resistance and capacitance from the secondary circuit changes while there is a contingency of misalignment. Subsequently, the data regarding the mutual inductance is more pertinent with the power transfer from one circuit to the next. From Fig. 8, it is inferred that the efficiency and voltage gain increases while there is an increase in the coupling coefficient. The efficiency increases from 79 to 93% for the proposed topology. Similarly, for the conventional LCL topology, the efficiency varies from 76 to 88.7%. The voltage gain of the proposed topology shifts from 0.65 to 1.57. Similarly, the conventional LCL voltage gain differs from 0.3 to 0.49. The variation in voltage gain of the conventional LCL topology is limited during the time of misalignment. The values of coupling factor vary from 0.1 to 0.3. In general, the power transfer efficiency increases while coupling coefficient progress. However, the voltage gain increases till the coupling coefficient reaches a certain level, after which the voltage gain decreases.

The simulation studies corroborate the notion of the theoretical aspect of the proposed model. The simulation case studies evaluate the feasibility of the proposed model under contingency in misalignment and variation in load.

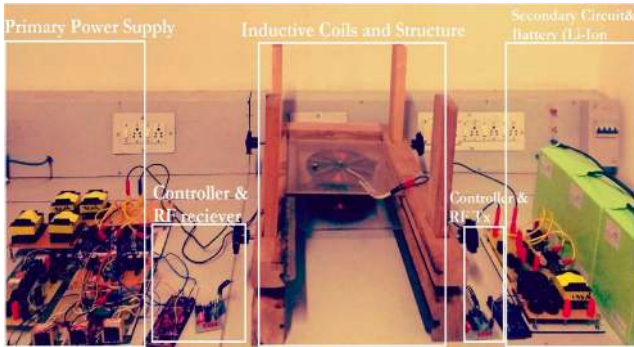


Fig. 9 Prototype of the proposed system

On comparison with the half and full H-bridge inverter, the proposed topology gives better performance in case of voltage gain during variation in mutual inductance and load variations.

4 Experimental studies

An experimental prototype of 1 kW is designed and developed for the validation of the proposed topology. The experimental prototype of the proposed system is shown in Fig. 9. Two MOSFET (SPW47N60C3) are used as switches S_1 and S_2 mentioned in the figure. High-frequency switching diodes (MUR1560G) has been used as semiconductor switches for uncontrolled bridge rectifier connected at the secondary side in the system. The inductive coils are vertically displaced by 16 cm with respect to each other.

The voltage across the primary inductor and the secondary pickup coil are shown in Fig. 10a. The primary coil draws RMS current of 25.5 A to deliver 1 kW at the load end, which is shown in Fig. 10b. The voltage across the charging inductor with respect to the primary coil voltage is shown in Fig. 10c. The current through the secondary inductor (I_s), voltage across the charging inductor and voltage across primary inductive (L_p) are shown in Fig. 10d. Secondary track current, voltage across the secondary parallel capacitor with respect to the V_{L_p} are shown in Fig. 11a. The voltage across the primary inductor with respect to the voltage across the capacitor C_{p1} is shown in Fig. 11b. Similarly, voltage across primary inductor, current through charging inductor (i_{L_c}) and voltage across charging inductor (V_{L_c}) is shown in Fig. 11c. Two gate pulses of 32% duty ratio and phase shift (t_d) of $T/2$ period is used to control the switches shown in Fig. 11d. The RMS value of voltage across charging inductor is same as the RMS value of voltage across capacitor C_{p1} . During the time of resonance, the term $1 - \omega^2 L_{seq} C_{sp}$ approaches to zero. According to (24), the angle ϕ approaches to $-\pi/2$, which indicates the secondary current is in phase with the primary inductive voltage. This is achieved in hardware during the time of resonance. Semiconductor switches have high current carrying capability connected with an external RCD snubber circuit for the dv/dt protection. Fast switching uncontrolled diode is used for the rectification purpose on the load side. Coaxial copper conductors are mounted on the ferrite spokes to enhance the flux linkage to the pickup coil. The obtained results substantiate that the proposed system performed well under perturbation in the parameter variations. The experimental setup operates at 85 kHz operating frequency to deliver 1 kW output power. From the results, it is inferred that the proposed topology is

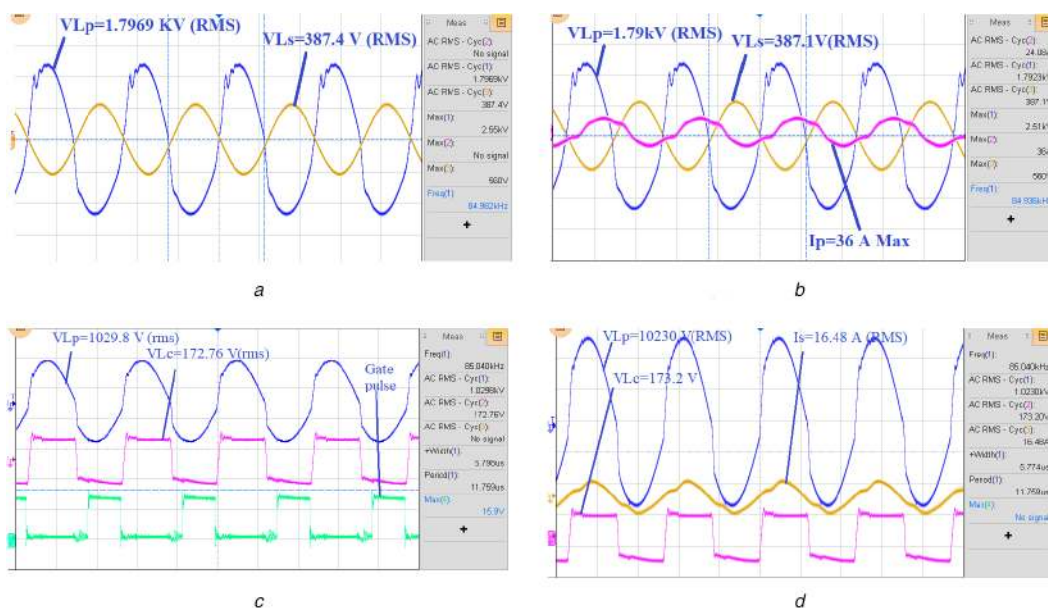


Fig. 10 Experimental waveform from the prototype

(a) V_{L_p} and V_{L_s} , (b) V_{L_p} , V_{L_s} and I_p , (c) V_{L_p} , V_{L_c} and V_G , (d) V_{L_p} , V_{L_c} and I_s

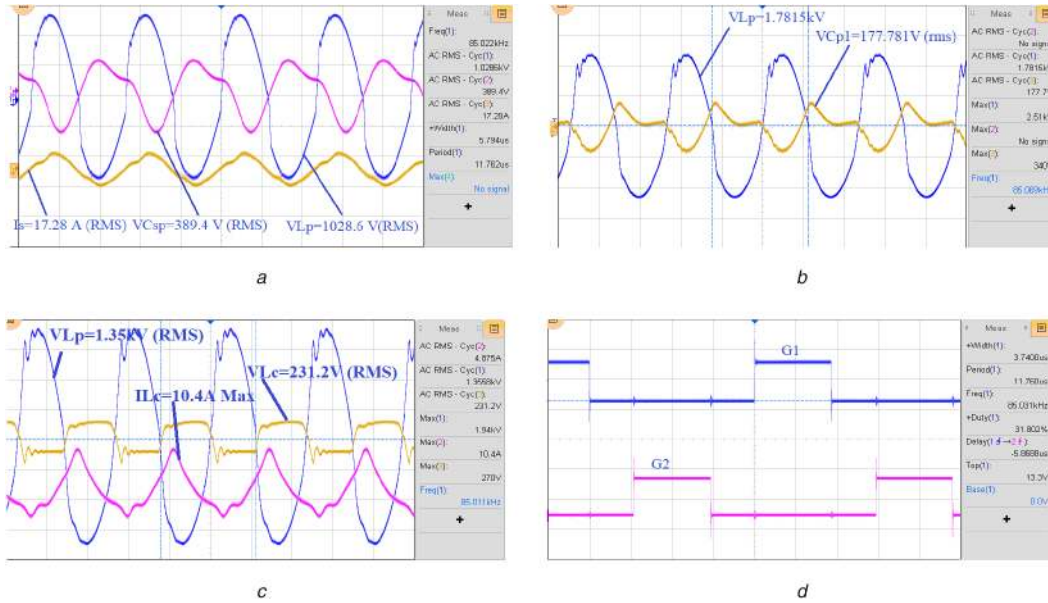


Fig. 11 Experimental waveform from the prototype
(a) V_{Lp} , V_{Csp} and I_s , (b) V_{Lp} and V_{Cp1} , (c) V_{Lp} , V_{Lc} and I_{Lc} , (d) Gate pulses

working well in lower switching frequency compared to the class E inverter. The system achieved an efficiency of 86.45% at 0.16 coupling. The secondary resonant circuit is attached to the pickup coil and is connected to the load.

4.1 Losses due to the semiconductor switches

Conduction and switching losses in semiconductor switches are very dominant in the system. A few amount of energy is dissipated as a heat in the internal resistance of inductor. In the proposed converter, time delay between the switches S_1 and S_2 decides the RMS value of the inductor voltage. The very same RMS value of current decides the conduction losses in the system. Hence, the time delay between the switches and the conduction losses are very much related. The values of circuit elements considered for the simulation and experimental study has been given in Table 1.

4.1.1 Conduction losses: Conduction losses occur in switches as well as other energy storage elements, which are practically not ideal in nature. There are I^2R losses that occur in the conduction path. The major conduction losses occur in the winding and in the switches during the time of current conduction. The conduction losses are estimated based on the values of the data sheet of the switches and the measured internal resistance of the inductors in the system. In this proposed system, MOSFET SPW47N60C3 is used as the switch. The internal resistance of the MOSFET is 0.07Ω . The RMS current drawn by the switch S_2 is 13 A to deliver 800 W power to the load. Hence, power 11.83 W is lost across the switch S_2 and 15.75 W is lost across S_1 .

4.1.2 Switching losses: The most dominant loss present in the system is switching losses, which is generally more than conduction losses. Presence of Zero Voltage Switching (ZVS) and snubber circuit reduce the switching losses to some extent. During the turn off time of the switches S_1 and S_2 , the alternative diodes D_1 and D_2 , respectively, are forward biased. This eventually transits the current conduction smoothly from switch to the diode. In other words, the current through the switch came to zero before the voltage rise across the switch, due to the delayed withdrawn of gate pulses. However, turn on switching losses will occur. To reduce the turn on losses, diode followed by capacitor combination is connected across the switch [27, 28]. The conventional ZVS switching has reduced the turn on switching losses by 85%.

The turn on switching losses are calculated based on (21)

$$P_{S_{on}} = I_{D(on)} V_{DD} f_{sw} \frac{t_{ri} t_{fv}}{2} \quad (28)$$

t_{ri} is the time taken to rise the current and t_{fv} is the time taken to fall voltage. Similarly, turn off losses is written as

$$P_{S_{off}} = I_{D(on)} V_{DD} f_{sw} \frac{t_{rv} t_{fi}}{2} \quad (29)$$

The total losses will be

$$P_{total} = P_{cond} + P_{on} + P_{off} \quad (30)$$

From (28) and (29), it is concluded that the total switching losses in the system is 24.84 W. In the overall system, the DC–DC efficiency is 86.45% at 0.16 coupling. This efficiency is maintained more or less throughout the coupling range from 0.1 to 0.3 in the proposed system.

5 Comparison to the predominant topologies

The prominent other topologies in the literature were compared with the proposed one. It is observed that the proposed topology gives a consistent efficiency under coupling coefficient variation corresponding to the load resistance variation. Sufficient parameters are considered for the comparison with the other predominant topologies. The voltage gain and efficiency of LCL, high gain LCL and proposed topology is plotted against the variation of coupling coefficient and load variation and are shown in Figs. 12a and b. Table 2 gives the values of different parameters for the different circuit topologies. Except for class E topology all other topologies are operated at 85 kHz and deliver 1 kW power to the load. Class E topologies transfer power in range of 5–50 W power with the resonance-enhanced IPT [29, 30]. This is because of the requirement of higher operating frequency to maintain higher quality factor. Otherwise, the efficiency of converter drastically reduces. The class E converter as it is cannot be used for electric vehicle charging applications due to the higher frequency of operation and limitation in higher power transfer capability. The inclusion of class E topology for comparison is to portray the benefits of proposed one over the other existing predominant topologies. However, the other parameter values may not be significant unless and until all the topologies are operated at same power and operating frequency.

The DC–DC voltage gain of high gain LCL topology at lower coupling coefficient is higher than that of LCL, class E, SLC and proposed system. Similarly, the voltage gain of proposed system is

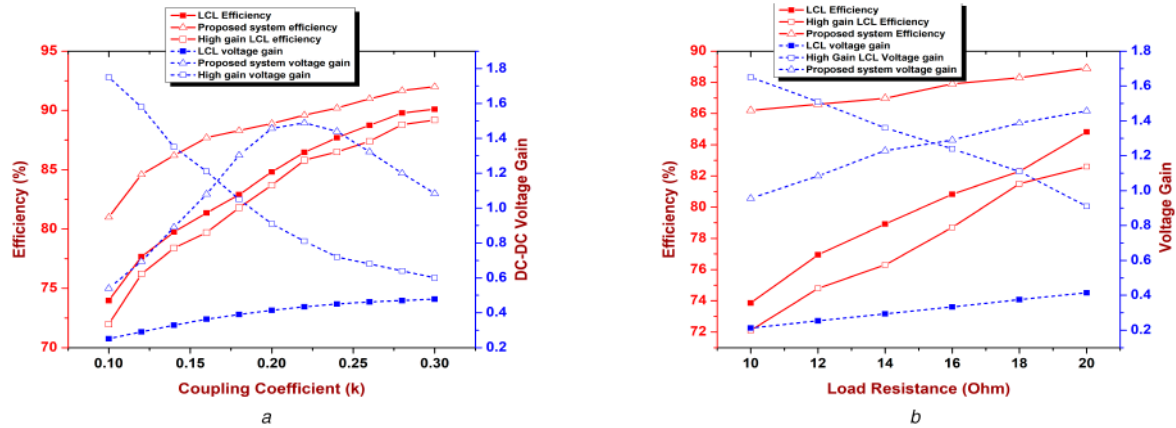


Fig. 12 Efficiency and voltage gain of various topologies

(a) Efficiency and voltage gain against coupling coefficient variation, (b) Efficiency and voltage gain against load resistance variation

Table 2 Comparison with other topologies

Parameter	LCL	Class E	High-gain LCL	SLC	Proposed system
power	1 kW	50 W	1 kW	1 kW	1 kW
frequency of operation (f)	85 kHz	1–6 MHz	85 kHz	85 kHz	85 kHz
efficiency	76–90%	85–95%	74–87%	76–90%	79–93%
voltage gain	0.25–0.5	0.7–1.1	0.6–2.1	0.3–0.7	0.5–1.8
No. of semiconductor devices	8	2	10	8	6
No. of energy storage elements	9	8	10	9	9
voltage stress across the switch (inverter)	$\frac{V_{dc}}{2}$	$2V_{dc}$	$\frac{V_{dc}}{2}$	$\frac{V_{dc}}{2}$	$2V_{dc}$
coupling coefficient variation for consistent operation	0.1–0.25	0.05–0.15	0.1–0.25	0.1–0.25	0.1–0.3
preferred load	heavy load	light load	heavy load	light load	both heavy and light load
complexity of power circuit and control in operation	not complex	complex in control	not complex	complex in control	not complex
compactness	not compact	very compact	not compact	not compact	compact
preferred for dynamic IPT	preferred	not preferred	preferred	preferred for light load	mostly preferred

higher than the other topologies at higher coupling coefficient. However, the efficiency of proposed system is higher than high gain LCL, LCL and SLC topology. High power transfer efficiency with lesser deviation is maintained with respect to the coupling coefficient range of 0.1–0.3. These attributes of proposed system make the system suitable for dynamic IPT.

6 Conclusion

The Proposed topology with reduced semiconductor switches gives better power transfer efficiency under lower coupling coefficients. The compactness of the system is improved when compared to the LCL-based IPT system due to the modified design of the energy storage element as well as proper utilisation of semiconductor devices. The various simulation case studies subjected to the misalignment and load variation corroborates the notion regarding the performance and operation of the system. This eventually portrays the consistency to maintain high power transfer efficiency as well as high voltage gain in comparison with the LCL-based IPT system. Similarly, the developed 1 kW experimental prototype outperforms the conventional LCL topology during the variations in load current and misalignment in the pickup coil.

7 Acknowledgment

The entire work is completely funded by the Department of science and technology (DST), SERB, Govt. of India (YSS/2015/001277). The entire research work is carried out at Vellore Institute of Technology- Chennai, research laboratory.

8 References

- [1] Esteban, B., Sid-Ahmed, M., Kar, N.C.: 'A comparative study of power supply architectures in wireless EV charging system', *IEEE Trans. Power Electron.*, 2015, **30**, (11), pp. 6408–6422
- [2] Wu, H.H., Gilchrist, A., Sealy, K.D., *et al.*: 'A high efficiency 5 kW inductive charger for EVs using dual side control', *IEEE Trans. Ind. Inf.*, 2012, **8**, (3), pp. 585–595
- [3] Boys, J.T., Covic, G.A.: 'The inductive power transfer story at the University of Auckland', *IEEE Circuit Syst. Mag.*, 2015, **15**, (2), pp. 6–27
- [4] Bosshard, R., Kolar, J.W.: 'Inductive power transfer for electric vehicle charging', *IEEE Power Electron. Mag.*, 2016, **3**, (3), pp. 22–30
- [5] Varikkottil, S., Febin Daya, J.L.: 'High-gain LCL architecture based IPT system for wireless charging of EV', *IET Power Electron.*, 2019, **12**, (2), pp. 195–203
- [6] Hui, S.Y.: 'Planar wireless charging technology for portable electronic products and Qi', *Proc. IEEE*, 2013, **101**, (6), pp. 1290–1301
- [7] Jabbar, H., Song, Y.S., Jeong, T.T.: 'RF energy harvesting system and circuits for charging of mobile devices', *IEEE Trans. Consum. Electron.*, 2010, **56**, (1), pp. 247–253
- [8] Sooraj, V.: 'A study of magnetic coupling and selection of operating frequency for static and dynamic EV charging system'. 2016 Int. Conf. on Circuit, Power and Computing Technologies (ICCPCT), Nagercoil, India, August 2016, pp. 1–4
- [9] Choi, S.Y., Gu, B.W., Jeong, S.Y., *et al.*: 'Advances in wireless power transfer systems for roadway-powered electric vehicles', *IEEE J. Emerg. Sel. Top. Power Electron.*, 2015, **3**, (1), pp. 18–36
- [10] Varikkottil, S., Febin Daya, J.L.: 'Estimation of optimal operating frequency for wireless EV charging system under misalignment', *Electronics*, 2019, **8**, (3), p. 342
- [11] Wang, C.-S., Stielau, O.H., Covic, G.A.: 'Design considerations for a contactless electric vehicle battery charger', *IEEE Trans. Ind. Electron.*, 2015, **52**, (5), pp. 1308–1314
- [12] Stergiou, C.A., Zaspalis, V.: 'Impact of ferrite shield properties on the low-power inductive power transfer', *IEEE Trans. Mag.*, 2016, **52**, (8), pp. 8401601–8401609
- [13] Bosshard, R., Iruretagoyena, U., Kolar, J.W.: 'Comprehensive evaluation of rectangular and double-D coil geometry for 50 kW/85 kHz IPT system', *IEEE J. Emerg. Sel. Power Electron.*, 2016, **4**, (4), pp. 1406–1415

- [14] Kürschner, D., Rathge, C., Jumar, U.: 'Design methodology for high efficient inductive power transfer systems with high coil positioning flexibility', *IEEE Trans. Ind. Electron.*, 2013, **60**, (1), pp. 372–381
- [15] Qu, X., Jing, Y., Han, H., *et al.*: 'Higher order compensation for inductive-power-transfer converters with constant-voltage or constant-current output combating transformer parameter constraints', *IEEE Trans. Power Electron.*, 2017, **32**, (1), pp. 394–405
- [16] Yao, Y., Liu, X., Wang, Y., *et al.*: 'Modified parameter tuning method for LCL/P compensation topology featured with load-independent and LCT-unconstrained output current', *IET Power Electron.*, 2018, **11**, (8), pp. 1483–1491
- [17] Feng, H., Cai, T., Duan, S., *et al.*: 'An LCC compensated resonance converter optimized for robust reaction to large coupling variation in dynamic wireless power transfer', *IEEE Trans. Ind. Electron.*, 2016, **63**, (10), pp. 6591–6601
- [18] Samanta, S., Rathore, A.K.: 'A new current-fed CLC transmitter and LC receiver topology for inductive wireless power transfer application: analysis, design, and experimental results', *IEEE Trans. Transp. Electrification*, 2014, **19**, (4), pp. 995–1002
- [19] Wang, C.-S., Covic, G.A., Stielau, O.H.: 'Investigating an LCL load resonant inverter for inductive power transfer applications', *IEEE Trans. Power Electron.*, 2014, **19**, (4), pp. 995–1002
- [20] Liu, S., Liu, M., Yang, S., *et al.*: 'A novel design methodology for high-efficiency current-mode and voltage-mode class-E power amplifiers in wireless power transfer systems', *IEEE Trans. Power Electron.*, 2017, **32**, (6), pp. 4514–4523
- [21] Nagashima, T., Wei, X., Bou, E., *et al.*: 'Steady-state analysis of isolated class E^2 converter outside nominal operation', *IEEE Trans. Ind. Electron.*, 2017, **64**, (4), pp. 3227–3238
- [22] Imura, T., Hori, Y.: 'Maximizing air gap and efficiency of magnetic resonant coupling for wireless power transfer using equivalent circuit and Neumann formula', *IEEE Trans. Ind. Electron.*, 2011, **58**, (10), pp. 4746–4752
- [23] Wang, C.-S., Covic, G.A., Stielau, O.H.: 'Power transfer capability and bifurcation phenomena of loosely coupled inductive power transfer systems', *IEEE Trans. Ind. Electron.*, 2004, **51**, (1), pp. 148–157
- [24] Zhang, W., Wong, S.-C., Tse, C.K., *et al.*: 'Load-independent duality of current and voltage outputs of a series- or parallel-compensated inductive power transfer converter with optimized efficiency', *IEEE J. Emerg. Sel. Power Electron.*, 2015, **3**, (1), pp. 137–146
- [25] Diekhans, T., De Doncker, R.W.: 'A dual-side controlled inductive power transfer system optimized for large coupling factor variations and partial load', *IEEE Trans. Power Electron.*, 2015, **30**, (11), pp. 6320–6328
- [26] Hao, H., Covic, G.A., Boys, J.T.: 'An approximate dynamic model of LCL-T-based inductive power transfer power supplies', *IEEE Trans. Power Electron.*, 2014, **29**, (10), pp. 5554–5567
- [27] Choe, H.-J., Chung, Y.-C., Sung, C.-H., *et al.*: 'Passive snubber for reducing switching-power losses of an IGBT in a DC-DC boost converter', *IEEE Trans. Power Electron.*, 2014, **29**, (12), pp. 6332–6341
- [28] Li, Y.-F., Sue, S.-M.: 'Exactly analysis of ZVS behaviour for class E inverter with resonant components varying'. IEEE Conf. on Industrial Electronics and Applications, Beijing, People's Republic of China, August 2011
- [29] Liu, M., Qiao, Y., Liu, S., *et al.*: 'Analysis and design of a robust class E^2 DC-DC converter for megahertz wireless power transfer', *IEEE Trans. Power Electron.*, 2017, **32**, (4), pp. 2835–2845
- [30] Nagashima, T., Wei, X., Bou, E., *et al.*: 'Steady-state analysis of isolated class- E^2 converter outside nominal operation', *IEEE Trans. Power Electron.*, 2017, **64**, (4), pp. 3227–3238